

# A planetary wave model for Saturn's 10.7-hour periodicities

C. G. A. Smith<sup>a,b</sup>, L. C. Ray<sup>b</sup>, N. A. Achilleos<sup>b</sup>

<sup>a</sup>*Physics Department, The Brooksbank School, Elland, West Yorkshire, UK, HX5 0QG*

<sup>b</sup>*Department of Physics and Astronomy, Centre for Planetary Sciences, University College London, Gower St., London WC1E 6BT*

---

## Abstract

A proposed resolution of the unexplained 10.7-hour periodicities in Saturn's magnetosphere is a system of atmospheric vortices in the polar regions of the planet. We investigate a description of such vortices in terms of planetary-scale waves. Approximating the polar regions as flat, we use theory developed originally by Haurwitz (1975) to find circumpolar Rossby wave solutions for Saturn's upper stratosphere and lower thermosphere. We find vertically propagating twin vortex solutions that drift slowly westwards at  $< 1\%$  of the deep planetary angular velocity and are thus ideal candidates for explaining the observed periodicities. To produce integrated field-aligned currents of the order of 1MA we require wind velocities of  $\sim 70\text{ms}^{-1}$ . A particular class of vertically propagating solutions are potentially consistent with wave energy being 'trapped' between the deep atmosphere and lower thermosphere, at altitudes suited to the production of the necessary field-aligned current systems.

*Keywords:* Atmospheres, dynamics, Aurorae, Ionospheres, Saturn,

---

*Email address:* [cgasmith@gmail.com](mailto:cgasmith@gmail.com) (C. G. A. Smith)

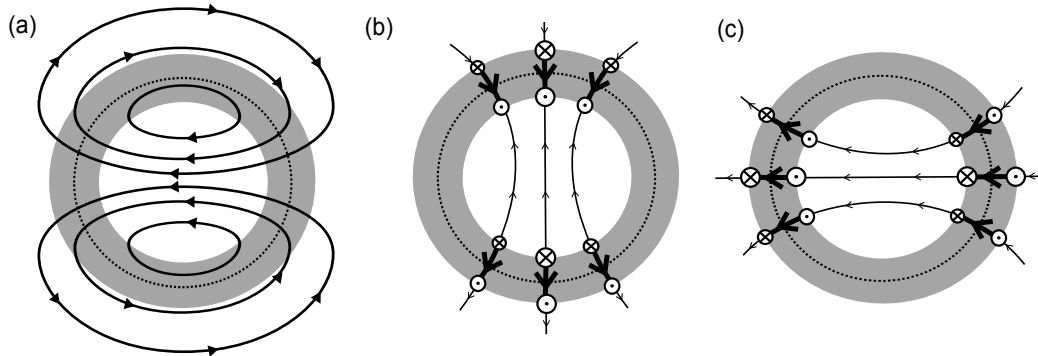


Figure 1: Sketches of the proposed vortex system. In each sketch the dotted line indicates the central line of the main auroral oval, and the shaded region the zone of enhanced ionisation associated with auroral electron precipitation. (a) Sketch of twin vortex flows. (b) Sketch of Pedersen currents. (c) Sketch of Hall currents.

atmosphere, Saturn, magnetosphere

---

## 1. Introduction

The  $\sim 10.7$ -hour modulation of various phenomena in Saturn's magnetosphere (see review by Carbary and Mitchell, 2013) has yet to be fully explained. The idea of a vortex-like structure in the neutral atmosphere driving magnetospheric periodicities was first proposed by Smith (2006) and investigated further by Smith (2011) and Smith and Achilleos (2012). The conclusion of these studies was that a thermospheric vortex could drive approximately the observed magnetic perturbations in the magnetosphere, but that the energy required to sustain magnetic perturbations of the observed magnitude was improbably large.

A complementary approach to the same conceptual model (Jia et al., 2012; Jia and Kivelson, 2012) imposed twin-vortex flows directly on the

13 ionospheric plasma and calculated the detailed implications for the magneto-  
14 sphere, using a magnetohydrodynamic model of this region. This approach  
15 reproduced many of the observed phenomena, but the thermospheric flow  
16 speeds prescribed by the model as a boundary condition were implausibly  
17 large. More recently, Southwood and Cowley (2014) presented a qualitative  
18 model of twin vortices in both northern and southern polar ionospheres, able  
19 to explain the ‘mixed’ northern and southern signals observed on closed field  
20 lines and the ‘pure’ northern and southern signals observed on open field  
21 lines.

22 Most recently, Smith (2014) synthesised the Southwood and Cowley (2014)  
23 model with lessons learnt from thermosphere modelling (Smith et al., 2005;  
24 Müller-Wodarg et al., 2006; Smith and Aylward, 2008; Smith, 2011; Smith  
25 and Achilleos, 2012), proposing that the vortices are located not in the ther-  
26 mosphere but in the upper stratosphere, around an altitude of  $\sim 750$ km above  
27 the 1-bar level. Two reasons were given for this suggestion. First, the po-  
28 lar thermosphere substantially subcorotates and so cannot sustain a vortex  
29 system with a steady  $\sim 10.7$ -hour rotation period. Second, a thermospheric  
30 vortex system of the required magnitude would entail an unrealistically large  
31 thermal energy input, the heating effect of which would produce thermo-  
32 spheric temperatures far greater than those that are observed.

33 A vortex system located in the upper stratosphere would interact with the  
34 ionisation produced at these altitudes by the particle precipitation associated  
35 with the main auroral oval, thus generating horizontally divergent currents  
36 that flow into and drive the magnetosphere. This scenario is sketched in  
37 Fig. 1. Panel (a) shows a simple twin-cell vortex system. Panels (b) and (c)

38 then indicate the currents driven by the interaction between these vortices  
39 and a region of enhanced conductance (indicated by the shaded regions).  
40 Panel (b) shows Pedersen currents and panel (c) Hall currents.

41 A number of studies have also examined empirical evidence for a neutral  
42 atmosphere source. Cowley and Provan (2013) examined the rotation periods  
43 of a number of neutral atmospheric features and searched for correlations with  
44 the observed periodicities in the magnetosphere. They found no convincing  
45 correlation that might indicate a direct causal link. Fischer et al. (2014)  
46 investigated a possible correlation between the presence of the Great White  
47 Spot in the northern hemisphere and a pronounced shift in the period of  
48 the 10.7-hour signal, but were unable to find a physical link between the  
49 two phenomena. While both of these studies were inconclusive, they dealt  
50 with tropospheric and lower stratospheric phenomena. They thus in no way  
51 rule out a source in the upper stratosphere or thermosphere. A different  
52 type of evidence was presented by Hunt et al. (2014) who analysed observed  
53 field-aligned currents in the southern auroral region, concluding that they  
54 provide evidence for energy flow outwards from the planet. This indicates an  
55 atmospheric location for the original source of energy. All of this evidence  
56 taken together – no evidence for a lower atmosphere source but positive  
57 evidence for an atmospheric source – points towards an upper atmosphere  
58 source as proposed by the recent theoretical studies referenced above (Jia  
59 et al., 2012; Southwood and Cowley, 2014; Smith, 2014).

60 Despite this evidence, as yet there has been no detailed model of how a  
61 twin vortex system could be generated or sustained in the upper atmosphere.  
62 A possible description of such a global vortex system is in terms of planetary-

63 scale waves. The purpose of this paper is to explore such a description of the  
64 required vortices in terms of circumpolar Rossby waves. In Section 2 we will  
65 outline how the properties of Rossby waves make them suitable candidates.  
66 In Section 3 we will then develop a theoretical description of circumpolar  
67 Rossby waves using the work of Haurwitz (1975). In Section 4 we will then  
68 analyse explicit solutions of our equations, including predictions of the mag-  
69 nitude of magnetospheric current systems produced. Finally, in Section 5 we  
70 will summarise and conclude.

## 71 **2. Outline of model**

72 In a rigidly rotating atmosphere, the restoring force mechanism for Rossby  
73 waves arises from the variation of the Coriolis parameter with latitude. In  
74 these circumstances they propagate westwards in the corotating frame at  
75 a small fraction of the planetary rotation velocity (e.g. Houghton, 1986).  
76 Rossby waves are thus good candidates for explaining the  $\sim 10.7$ -hour peri-  
77 odicities because, provided the background atmosphere on which they prop-  
78 agate is almost in rigid corotation with the deep atmosphere, they will also  
79 almost corotate with the deep atmosphere.

80 Furthermore, there is evidence that the  $\sim 10.7$ -hour periodicities corre-  
81 spond to angular velocities slightly slower than the deep rotation velocity of  
82 the planet (Gurnett et al., 2010), consistent with a small westwards prop-  
83 agation velocity. The westwards motion of Rossby waves in these circum-  
84 stances also suggests that Rossby waves in the already strongly subcorotat-  
85 ing thermosphere region are unlikely to be responsible for the periodicities: a  
86 westwards-propagating Rossby wave superimposed on the already westwards-

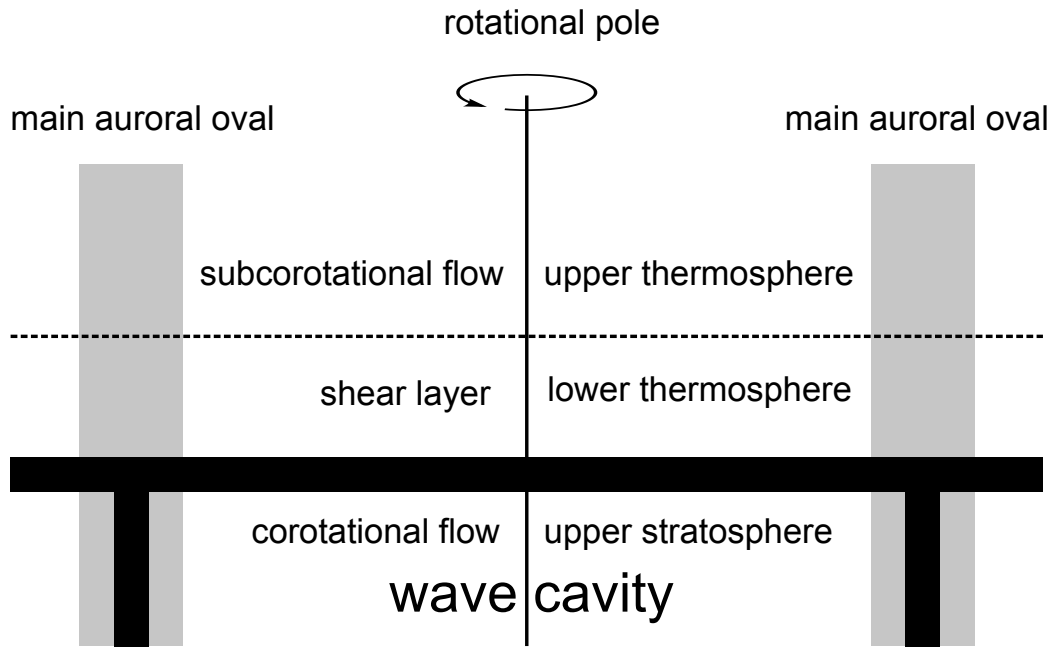


Figure 2: Sketch of proposed ‘wave cavity’ in the polar regions. The grey shaded area show the regions where ion densities are enhanced by ‘hard’ particle precipitation related to the main auroral oval. The black regions show the constraints of the wave cavity. The horizontal black bar is the ‘lid’ beyond which Rossby waves cannot propagate because the flow is strongly sheared westwards in the planet’s corotating reference frame. The vertical black bars are the locations where zonal winds are expected to be inhibited by relatively strong ion drag.

87 flowing gas at these altitudes would not have a  $\sim 10.7$ -hour period.

88 If the atmosphere is not rigidly rotating – i.e. if the zonal winds vary  
89 rapidly with latitude – then these attractive properties of Rossby waves break  
90 down. For example, within a strongly curved eastward jet Rossby waves may  
91 propagate with an eastwards phase velocity. We require a structure that  
92 slowly moves westwards, and therefore suitable  $\sim 10.7$ -hour Rossby waves  
93 must be located in regions where there are no strong jet curvatures and  
94 where the atmosphere is close to rigid rotation.

95 The troposphere and lower stratosphere are most certainly not suitable  
96 locations, with strongly curved jet structures observed at pressures higher  
97 than 100Pa (e.g. Read et al., 2009a). However, the altitudes of interest here,  
98 in the upper stratosphere and lower thermosphere, are at pressures around  
99 0.01Pa or less, or  $\sim 10$  pressure scale heights higher than the observed jets.  
100 We would not expect these jet structures to penetrate to such high altitudes.  
101 For example, Conrath et al. (1990) calculated mean flows in the stratosphere  
102 using a simple model that was forced by tropospheric jets as a lower boundary  
103 condition. The magnitude of the jets decayed with altitude – roughly in  
104 proportion to the pressure – indicating that their magnitude will be negligible  
105 in the upper stratosphere.

106 Instead, we would expect the dominant process forming zonal winds in  
107 the polar regions of the lower thermosphere and upper stratosphere to be  
108 the steady westwards drag of the magnetosphere on the thermosphere. This  
109 causes a continuous input of westwards momentum that must be transferred  
110 downwards to the deep atmosphere. This implies a vertically sheared struc-  
111 ture to the zonal flow, with the shear weakening with depth.

112 As a first approximation, we will assume that this shear is consistent with  
113 rigid rotation at each altitude. This means that at each altitude we treat the  
114 atmosphere as a rigidly rotating shell, with the westwards angular velocity of  
115 this shell decreasing with decreasing altitude. There are no direct measure-  
116 ments of neutral winds to support this model, however Doppler observations  
117 of the ion flows (e.g. Stallard et al., 2004) indicate approximately linear vari-  
118 ation of the zonal ion flows as a function of latitude, consistent with rigid  
119 rotation. These rigidly rotating zonal ion flows then directly drive the zonal  
120 neutral winds, and so it is likely that they will also be close to rigid rotation.

121 There is expected to be some localised curvature of the zonal flows close  
122 to the main auroral oval (Cowley et al., 2008) that will certainly violate the  
123 assumption of rigid rotation in the thermosphere. However, deeper in the  
124 atmosphere as the shear weakens we can expect this to be less important.  
125 We will thus provisionally assume rigid rotation as a simple background  
126 condition, even though it is unlikely to be exactly true throughout our region  
127 of interest.

128 The natural location for suitable  $\sim 10.7$ -hour Rossby waves is thus the  
129 region just below the thermosphere, in the altitude range 600-900km, as  
130 identified by Smith (2014). This region is expected to exhibit weak shear  
131 in zonal velocity as a function of altitude, as stated above, but still to be  
132 close to corotation, and so a westwards propagating Rossby wave would also  
133 only slightly lag corotation. Indeed, the existence of a strong rotational  
134 shear immediately above these altitudes indicates that Rossby waves existing  
135 below the shear layer could not propagate significantly to higher altitudes.  
136 In order to do so and remain coherent, the waves would require an eastward

137 phase velocity to counteract the background westward flow. For westward  
138 propagating Rossby waves such vertical propagation is impossible (unless  
139 the Rossby waves can couple to an eastward propagating wave of a different  
140 type). This suggests that the shear layer will act effectively as a ‘lid’ that  
141 inhibits the propagation of Rossby waves into the thermosphere.

142 Another important structure in the polar regions is the main auroral oval,  
143 which we take to lie at an approximate distance  $r_0 = 1.5 \times 10^7$  m from the  
144 pole, corresponding to a colatitude of  $\sim 16^\circ$  and a polar radius of  $\sim 54,000$   
145 km, consistent with the UV and IR auroral locations determined by Nichols  
146 et al. (2009) and Badman et al. (2011). This region is subject to precipitation  
147 by much more energetic electrons compared to the bulk of the polar cap. For  
148 example, Galand et al. (2011) modelled electron energies of 500eV for ‘diffuse’  
149 auroral emissions and 10keV for the ‘hard’ electron precipitation in the main  
150 auroral oval. This difference is significant, because in our altitude range of  
151 interest there is much greater electron density at the location of the main  
152 auroral oval, since the ‘hard’ electrons in this region penetrate deeper into the  
153 atmosphere, resulting in ionisation as deep as 700km altitude (Galand et al.,  
154 2011). Thus we expect significantly greater ion drag at these latitudes. Since  
155 the auroral oval lies very nearly along lines of constant latitude, one would  
156 expect the zonal component of any wind structure to be more significantly  
157 inhibited by ion drag than the meridional component: if the wind has a  
158 dominant zonal component at these latitudes then any particular parcel of gas  
159 will spend longer in the region of enhanced ion drag. Therefore the presence  
160 of the main oval should inhibit wave modes with strong zonal components at  
161 that latitude, producing a nodal line in the zonal wind perturbation at the

162 latitude of the main oval.

163 These considerations lead to the notion of an open ‘wave cavity’ in the  
164 polar regions, in which the thermospheric shear layer acts as the ‘lid’ and  
165 the main auroral oval as the ‘walls’. This situation is sketched in Fig. 2.  
166 The purpose of this paper will be to seek Rossby wave solutions in this  
167 cavity, and analyse whether they are suitable candidates for explaining the  
168 magnetospheric periodicities.

### 169 **3. Details of model**

#### 170 *3.1. Theory*

171 The description of global-scale planetary waves is achieved using tidal the-  
172 ory (e.g. Lindzen and Chapman, 1969). However, full solutions of Laplace’s  
173 tidal equation are complicated. It is thus common to analyse specific sit-  
174 uations using simplified geometries. At equatorial and mid-latitudes, wave  
175 modes can be analysed using a beta-plane approximation (in which the spher-  
176 ical geometry is neglected and the variation of the Coriolis parameter with  
177 latitude is approximated as linear). One such analysis was carried out by  
178 Lindzen (1967). We are chiefly interested in waves close to the poles, for  
179 which a standard beta-plane approximation is poor. This situation was anal-  
180 ysed by Haurwitz (1975) by approximating the polar regions as flat. We will  
181 apply this theoretical analysis to Saturn. The paper by Haurwitz uses some-  
182 what archaic notation and so, for clarity, we repeat the derivation using more  
183 modern notation (closely similar to that employed by Lindzen (1967)), with  
184 as much detail as possible presented in the Appendix, reserving the main  
185 results and a discussion of the important assumptions for the main text.

186 We assume that in its basic, unperturbed state the polar upper atmo-  
 187 sphere is isothermal, in hydrostatic equilibrium and rigidly rotating. The  
 188 observed neutral temperature in the stratosphere does not vary significantly  
 189 with altitude, lying approximately in the range 134-143K in the altitude range  
 190 350-850km (Moses et al., 2000). A constant value of  $\sim 140\text{K}$  thus seems ap-  
 191 propriate. We choose to use a constant temperature of  $T_0 = 144\text{K}$ , because  
 192 taking the gravitational field strength to be  $12\text{ms}^{-2}$  and the composition to  
 193 be pure  $\text{H}_2$ , this implies a round atmospheric scale height of 50km.

194 Also related to the temperature and significant for the theory that follows  
 195 is the value of  $\gamma = c_p/c_v$ , the ratio of specific heats. For a diatomic gas at  
 196 room temperature this is equal to 1.4. However, below a temperature of  
 197  $\sim 250\text{K}$  the rotational states of diatomic hydrogen are not fully populated  
 198 and so the specific heat capacity falls, approaching that of a monatomic gas  
 199 at  $\sim 50\text{K}$ , for which  $\gamma = 1.67$  (e.g. Sears and Salinger, 1975). Assuming an  
 200 ortho:para ratio of 3:1, the appropriate intermediate value is close to  $\gamma = 1.5$   
 201 (Leachman et al., 2009) and we adopt this value.

202 The physical quantities describing the basic state are the unperturbed  
 203 pressure, density and temperature  $p_0$ ,  $\rho_0$  and  $T_0$ , which are linked by vertical  
 204 force balance

$$\frac{\partial p_0}{\partial z} = -\rho_0 g \quad (1)$$

205 and by the equation of state of an ideal gas

$$p_0 = \rho_0 R_m T_0 / \mu = \rho_0 g H \quad (2)$$

206 where  $R_m$  is the molar gas constant,  $\mu = 2.0 \times 10^{-3}\text{kg}$  is the molar mass  
 207 of molecular hydrogen and  $H$  is the pressure scale height. These equations

208 taken together imply that, for our isothermal region, both  $p_0$  and  $\rho_0$  fall  
 209 exponentially with altitude  $z$  and with scale height  $H$ , i.e.

$$p_0 = p_{00}e^{-\Delta z/H} \quad (3)$$

$$\rho_0 = \rho_{00}e^{-\Delta z/H} \quad (4)$$

210 where  $\Delta z = z - z_{00}$ . We take  $p_{00} = 1.7 \times 10^{-3}\text{Pa}$ , the approximate pressure  
 211 at  $z_{00} = 900\text{km}$  above the 1-bar level in the Moses et al. (2000) model of the  
 212 neutral atmosphere. Note that because we assume a constant value of the  
 213 background temperature, the pressures at altitudes other than 900km do not  
 214 correspond exactly to those in the Moses et al. (2000) model.

215 The planet's 1-bar pressure surface may be approximated as an ellipsoid  
 216 with polar radius  $R_p \sim 54,000\text{km}$  and equatorial radius  $R_e \sim 60,000\text{km}$ . In  
 217 this situation the polar regions are well approximated as a spherical surface  
 218 with radius of curvature  $R_c = R_e^2/R_p \simeq 67,000\text{km}$ . The Coriolis parameter  
 219  $f$  is then given by:

$$f = 2\Omega \cos \frac{r}{R_c} \simeq 2\Omega \left(1 - \frac{r^2}{2R_c^2}\right) \quad (5)$$

220 where  $r$  is the radial distance from the pole along the curved surface of the  
 221 planet. We take  $\Omega \simeq 1.65 \times 10^{-4}\text{rads}^{-1}$  to be the deep planetary angular  
 222 velocity. We have derived this value by averaging the two independent de-  
 223 terminations of the rotation period by Anderson and Schubert (2007) and  
 224 Read et al. (2009b).

225 To further simply matters we can approximate the polar regions as flat.  
 226 To do so we use the approximate expression for  $f$  given above, but take  
 227  $r$  to represent the radial coordinate in cylindrical polar coordinates. We

228 investigate a situation centred around the north pole, so that  $r$  is in the radial  
 229 direction (equatorwards),  $\phi$  is eastwards (anti-clockwise viewed from above  
 230 the north pole) and  $z$  is vertically upwards. An analysis of the significance of  
 231 approximating the polar regions as flat was presented by Bridger and Stevens  
 232 (1980). They found that while there were some small quantitative differences  
 233 in modelling the polar regions as flat rather than curved, the same qualitative  
 234 wave behaviour was observed. The approximation is thus clearly reasonable  
 235 for this initial study.

236 We then introduce perturbations to the three-component neutral wind ( $u$ ,  
 237  $v$  and  $w$  representing eastward, northward and upward winds respectively)  
 238 and to the pressure and density ( $\delta p$ ,  $\delta \rho$ ). We do not explicitly denote the  
 239 wind perturbations with a ‘ $\delta$ ’ because the unperturbed wind is zero in our  
 240 rigidly rotating frame of reference. These perturbations are assumed to be  
 241 sufficiently small that second-order terms can be neglected. The horizontal  
 242 momentum equation yields the first two equations, vertical force balance the  
 243 third, continuity the fourth and energy conservation the fifth:

$$\frac{\partial u}{\partial t} - fv = -\frac{1}{\rho_0} \frac{1}{r} \frac{\partial \delta p}{\partial \phi} \quad (6)$$

244

$$\frac{\partial v}{\partial t} + fu = \frac{1}{\rho_0} \frac{\partial \delta p}{\partial r} \quad (7)$$

245

$$\frac{\partial \delta p}{\partial z} = -g\delta \rho \quad (8)$$

246

$$\frac{\partial \delta \rho}{\partial t} + w \frac{\partial \rho_0}{\partial z} + \rho_0 \left( \frac{1}{r} \frac{\partial u}{\partial \phi} - \frac{1}{r} \frac{\partial vr}{\partial r} + \frac{\partial w}{\partial z} \right) = 0 \quad (9)$$

247

$$\frac{\partial \delta p}{\partial t} + w \frac{\partial p_0}{\partial z} = \gamma g H \left( \frac{\partial \delta \rho}{\partial t} + w \frac{\partial \rho_0}{\partial z} \right) + q \rho_0 (\gamma - 1) \quad (10)$$

248 The symbol  $q$  represents the rate of external thermal energy input per unit  
 249 mass. We have included this function to maintain the generality of our  
 250 derivation, but in this study we will only consider free oscillations that are  
 251 not continuously forced. In the third equation we have assumed hydrostatic  
 252 equilibrium holds and thus neglected vertical accelerations of the neutral gas.  
 253 It is noted that these equations are closely analogous to Eqns. 1-5 of Lindzen  
 254 (1967).

255 We further assume that all of these perturbation variables, and the heat-  
 256 ing function  $q$ , vary as

$$e^{i(\omega t + k\phi)} \quad (11)$$

257 Note that for positive  $\omega$  and positive  $k$  this indicates a wave with phase  
 258 velocity

$$c = -\omega/k \quad (12)$$

259 so phase fronts propagate in the negative  $\phi$  direction, i.e. westwards. We will  
 260 assume positive  $k$  throughout, so that eastward phase propagation is implied  
 261 by negative values of  $\omega$ .

262 The analysis then proceeds as described in the Appendix, by combining  
 263 Eqns 6-10 and then separating variables. The following points from the  
 264 derivation are worth restating here:

- 265 1. A separation constant  $h$  is introduced, commonly referred to as the  
 266 ‘equivalent depth’. This parameter characterises each wave mode and  
 267 links their horizontal and vertical structure.

268 2. To simplify the equations we require that  $\epsilon^2 r^2 \ll 1$  where

$$\epsilon^2 = \frac{\omega^2}{ghk^2} \quad (13)$$

269 This assumption will be justified further below.

270 3. To simplify the equations we assume a constant Coriolis parameter  
271 which we calculate at the location of the main auroral oval ( $r_0 = 1.5 \times$   
272  $10^7$ m):

$$f_0 = 2\Omega \left( 1 - \frac{r_0^2}{2R_c^2} \right) \quad (14)$$

273 with the exception of a single term that depends upon the radial deriva-  
274 tive of  $f$ , for which we use the approximate value:

$$\frac{\partial f}{\partial r} \simeq -\frac{2\Omega r}{R_c^2} \quad (15)$$

275 This is a type of beta-plane approximation.

276 Once these approximations are made, the part of the solution that represents  
277 variation in the  $r$  direction turns out to satisfy Bessel's equation, provided  
278 that a parameter  $m$  is given by

$$m^2 = \frac{2\Omega k}{R_c^2 \omega} - \frac{(f_0^2 - \omega^2)}{gh} - \frac{2f_0 \omega}{ghk} \quad (16)$$

279 This yields the following expressions for the perturbation variables (noting  
280 again that we are ignoring the forcing function  $q$ , such that these expressions

281 are appropriate for free oscillations only):

$$u = -iu_0 J'_k(mr) F(z) e^{z/2H} e^{i(\omega t + k\phi)} \quad (17)$$

$$v = v_0 \frac{J_k(mr)}{mr} F(z) e^{z/2H} e^{i(\omega t + k\phi)} \quad (18)$$

$$\delta p = -i\delta p_0 K_k(mr) F(z) e^{-z/2H} e^{i(\omega t + k\phi)} \quad (19)$$

$$\delta \rho = -i\delta \rho_0 K_k(mr) \left[ \frac{F(z)}{2} - HF'(z) \right] e^{-z/2H} e^{i(\omega t + k\phi)} \quad (20)$$

$$w = w_0 K_k(mr) \left[ \left( \frac{1}{2} - \frac{1}{\gamma} \right) F - HF' \right] e^{z/2H} e^{i(\omega t + k\phi)} \quad (21)$$

282 The function  $F$ , to be discussed in Section 3.4, defines the vertical structure.

283 The function  $K_k$  is given by

$$K_k(mr, \omega) = J_k(mr) - \frac{\omega mr}{f_0 k} J'_k(mr) \quad (22)$$

284 Provided that  $\omega \ll f$  (true for all slowly propagating solutions that are  
 285 relevant here) and if  $mr$  and  $k$  are of order unity (also true for all situations  
 286 considered here), the second term in the equation for  $K_k$  is much smaller  
 287 than the first and thus  $K_k \simeq J_k$ .

288 The various constants  $u_0$  etc., which describe the perturbation ampli-  
 289 tudes, are related by defining characteristic horizontal and vertical speeds  
 290  $u_{00}$ ,  $v_{00}$  and  $w_{00}$  given by:

$$v_{00} = \frac{mkgH}{f_0} = ku_{00} \quad w_{00} = \frac{\omega H}{\kappa} \quad (23)$$

291 where  $\kappa = (\gamma - 1)/\gamma$ . This allows us to write the following simple expression:

292

$$\frac{w_0}{w_{00}} = \frac{\delta p_0}{p_0} = \frac{\delta \rho_0}{\rho_0} = \frac{u_0}{u_{00}} = \frac{v_0}{v_{00}} \quad (24)$$

293 *3.2. Horizontal structure*

294 We now apply these solutions to Saturn. The equations above permit a  
 295 continuous spectrum of wave modes with different values of  $k$  and  $m$ . We  
 296 are interested in wave modes with  $k = 1$  (commonly referred to as ‘ $m = 1$ ’ in  
 297 the context of magnetospheric periodicities, because  $m$  is the usual label for  
 298 the longitudinal wave number when considering spherical harmonics). This  
 299 restricts us to solutions involving the first order Bessel function  $J_1$ . Next, we  
 300 note our proposed condition that the zonal wind is inhibited at the latitude  
 301 of the main auroral oval, due to the increased ion drag at this latitude. Thus  
 302 the wave mode with  $u(r_0) = 0$  is preferred. This occurs when  $J'_1(mr_0) = 0$ .  
 303 This is true if  $mr_0 = j_0$ , where  $j_0 = 1.841$ , and this gives us a unique value  
 304 for  $m = 1.23 \times 10^{-7} \text{m}^{-1}$ . We can now calculate a value of  $v_{00} \simeq 230 \text{ms}^{-1}$  for  
 305 this situation.

306 Fig. 3 shows the variation of  $J_1(x)$ ,  $J'_1(x)$ , and other functions that ap-  
 307 pear in our solutions, where in this case  $x$  corresponds to the dimensionless  
 308 parameter  $mr$ . The mapping to  $r$  for our specific situation is shown on the  
 309 upper axis. This shows the main auroral oval at  $r = 1.5 \times 10^7 \text{m}$  correspond-  
 310 ing to the first zero in  $J'_1(x)$ . This is the first nodal line in the zonal winds.  
 311 The next significant radius is  $r = 3.1 \times 10^7 \text{m}$ , corresponding to the first zero  
 312 in  $J_1(x)$ . This is the first nodal line in the meridional winds.

313 The triple-dot-dash line shows  $K_1$  when  $\omega/f_0k = 0.1$ , corresponding to  
 314 a wave speed of  $\sim 20\%$  of the planetary rotation. This is not significantly  
 315 different from the curve for  $J_1$ , showing that the second term of  $K_1$  (Eqn 22)  
 316 is relatively small. For realistic values of the wave speed that are at least  
 317  $\sim 100$  times smaller, the curves for  $J_1$  and  $K_1$  are almost indistinguishable.

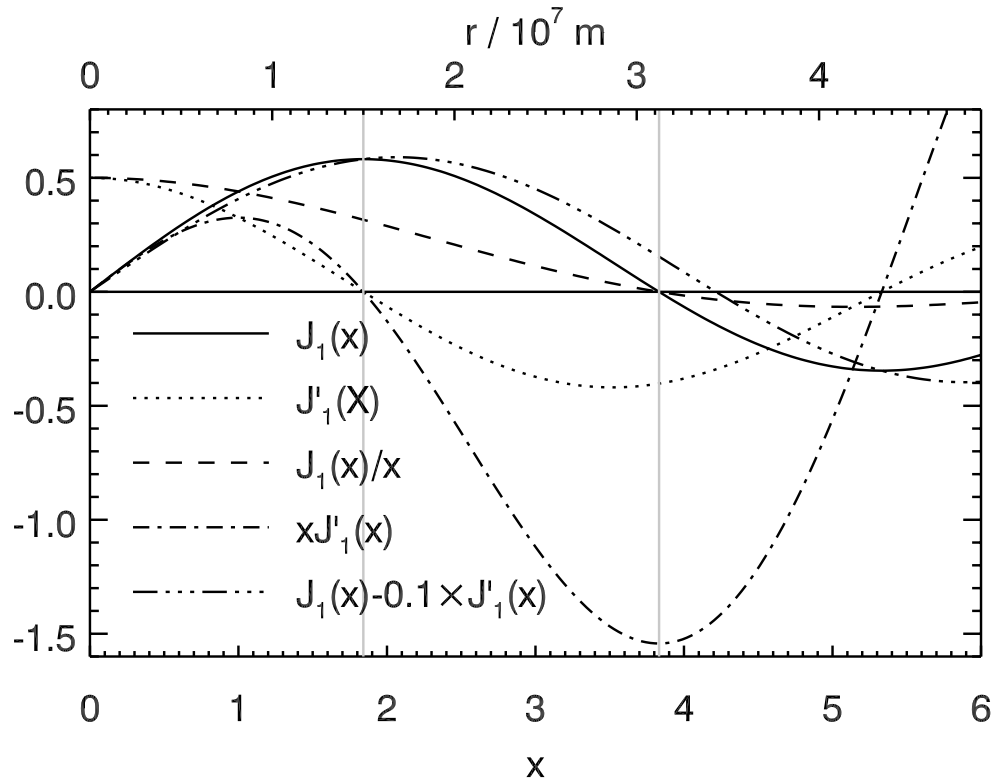


Figure 3: Horizontal structure functions. The solid and dotted lines show the Bessel function  $J_1$  and its first derivative. The other lines show various combinations of these functions, as indicated in the key. The vertical grey lines show the locations of the first zeroes in  $J_1$  and  $J_1'$ .

318 We now plot the horizontal structure of the solutions. We take a value of  
319  $F(z) = 1$  so that the plots represent a snapshot at any altitude, and  $v_0 = 1$   
320 so that the plots can easily be scaled to more complex situations.

321 Fig. 4 then shows views from above the north pole, with the location of  
322 the first zeroes in  $J_1$  and  $J'_1$  shown with the circular dot-dash lines. Panel  
323 (a) shows the horizontal flow pattern using unscaled arrows. This represents  
324 precisely the type of twin-vortex flow that has been proposed to explain the  
325 10.7-hour periodicities. Panel (b) shows the magnitude of the velocity at  
326 each location as a contour plot. The maximum velocity perturbation when  
327  $v_0 = 1\text{ms}^{-1}$  is at the pole, and has a value just below  $0.5\text{ms}^{-1}$ . Panel (c) shows  
328 the horizontal distribution of the pressure perturbation. This is proportional  
329 to  $K_1$  but for all solutions discussed here it is dominated by  $J_1$  so that the  
330 plot is indistinguishable from a plot involving the term in  $J_1$  alone. Taken  
331 together, these plots indicate that the wind perturbation is essentially a two  
332 cell circulation around regions of high and low pressure which drifts slowly  
333 westwards.

334 We can further calculate the pattern of field-aligned currents. The cur-  
335 rents generated will depend on the distribution of  $F(z)$  with altitude. How-  
336 ever, the overall pattern should be the same at all altitudes. We therefore  
337 take  $F(z) = 1$  and  $v_0 = 1\text{ms}^{-1}$  again to perform a baseline calculation of the  
338 currents. As discussed by Smith (2014) the primary process for producing  
339 field-aligned currents in the upper stratosphere is the horizontal divergence  
340 of the Hall current. We calculate these currents for the altitude range 700-  
341 900km, assuming a vertically uniform electron density in this region, but we  
342 allow it to vary with latitude to represent the enhanced electron density in

343 the region of the main auroral oval:

$$n = n_0 \left( 1 + 100 \times \exp \left[ \frac{(r - r_0)^2}{2W^2} \right] \right) \quad (25)$$

344 Here a background electron density  $n_0 = 5 \times 10^8 \text{m}^{-3}$  is enhanced by a factor  
345 of  $\sim 100$  in the region of the main auroral oval. The region of enhancement  
346 is represented by a gaussian of FWHM  $\sim 1000 \text{km}$ , defined by  $W = 400 \text{km}$ .  
347 This distribution is shown in Fig. 4d. The value of  $W$  has little effect on  
348 the total field-aligned current because the integrated divergence depends on  
349 the maximum value of the enhanced electron density, not on its horizontal  
350 distribution. The values of the background and enhanced electron densities  
351 are based on the results of Galand et al. (2011) and are discussed in Smith  
352 (2014).

353 Using this expression for  $n$  we calculate profiles of Pedersen and Hall  
354 conductivity using the expressions given by Smith (2013) and Smith (2014).  
355 We use  $B = 60000 \text{nT}$  for the polar magnetic flux density. We then calcu-  
356 late the horizontal Pedersen and Hall currents and their height-integrated  
357 divergences. The resulting field-aligned currents are shown in Fig. 4e (for  
358 the background electron density only) and Fig. 4f (for the enhanced elec-  
359 tron density). The background electron density produces two broad areas  
360 of relatively low field-aligned current. These are the currents predicted by  
361 the model of Southwood and Cowley (2014), which assumes a uniform back-  
362 ground conductance. These are mostly due to divergence of the Pedersen  
363 current. In contrast, the enhanced electron density produces two pairs of  
364 upwards- and downwards-directed current sheets either side of the main au-  
365 roral oval. These are mostly due to divergence of the Hall current.

366 If we integrate the field-aligned current across any of the four current  
 367 sheets shown in Fig. 4f, we find a total value of  $\sim 0.06\text{MA}$ . This is an order of  
 368 magnitude lower than that required to explain the periodicities. The current  
 369 scales linearly with wind speed, indicating that we will require higher wind  
 370 speeds than  $v_0 = 1\text{ms}^{-1}$  to produce the required currents. The assumption  
 371 that  $F(z) = 1$  also probably overestimates the total current, because  $F(z)$  is  
 372 likely to vary with altitude. More complete calculations will be presented in  
 373 Section 4.

### 374 3.3. Horizontal propagation

375 Fig. 4 demonstrates that our proposed wave structure produces the cor-  
 376 rect circulation pattern and the correct general pattern of field-aligned cur-  
 377 rents required to explain the magnetospheric periodicities. We must now  
 378 establish whether the pattern rotates with an appropriate value of  $\omega$ . Sub-  
 379 stituting  $m = j_0/r_0$  into Eqn. 16 gives a cubic equation for  $\omega$  in which the  
 380 only free parameter is the separation constant  $h$ :

$$\omega^3 - 2f_0\omega^2 - \left(f_0^2 + \frac{j_0^2gh}{r_0^2}\right)\omega + \frac{2\Omega gh}{R_c^2} = 0 \quad (26)$$

381 Fig. 5a shows how the possible values of  $\omega$  vary for different values of  
 382  $h$ . Solid lines show real solutions for  $\omega$ . Each region of the real solutions is  
 383 labelled with a letter from A to E. Complex solutions are shown by dashed  
 384 lines (showing the real parts) and pairs of dotted lines (showing the two con-  
 385 jugate imaginary parts of the two complex solutions). The horizontal shaded  
 386 region (only just visible as a thin line at  $\omega = 0$ ) shows  $\pm 0.01\Omega$ , i.e. modes  
 387 that propagate at  $\sim 1\%$  of the planetary rotation velocity must lie within this  
 388 region.

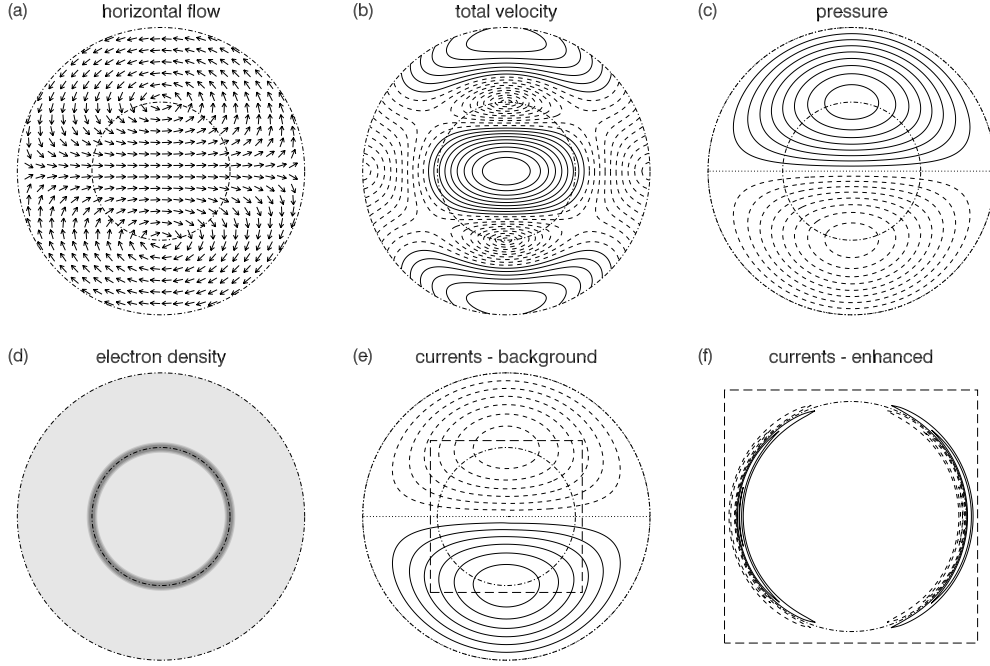


Figure 4: In all plots the dash-dot lines show the location of the first zero in  $J_1'$  (at  $r = 1.5 \times 10^7 \text{m}$ ) and the first zero in  $J_1$  (at  $r = 3.1 \times 10^7 \text{m}$ ). In panels (a)-(c) the data are for  $v_0 = 1$  and  $F(z) = 1$  at  $z = 900 \text{km}$ . In panels (e) and (f) the currents have been integrated across the range  $z = 700 - 900 \text{km}$  based on the same assumptions. (a) Horizontal flow pattern. Arrows are not scaled. (b) Total flow velocity. Dashed contours show flow speeds less than or equal to  $0.25 \text{ms}^{-1}$  with a spacing of  $0.025 \text{ms}^{-1}$ . Solid contours show greater flow speeds, with the same spacing. (c) Pressure perturbation. Solid and dashed lines show positive and negative values. Dotted lines show zero contours. The contours are spaced at intervals of  $5 \times 10^{-8} \text{Pa}$ . The maximum pressure perturbation contour shown is  $4 \times 10^{-7} \text{Pa}$ . (d) Electron density model. A uniform background density (light grey) with a narrow enhanced region at the location of the main oval (dark grey). (e) Field-aligned currents calculated using the background electron density only. Solid and dashed lines show positive and negative values. Dotted lines show zero contours. The contours are spaced at intervals of  $5 \times 10^{-6} \text{nAm}^{-2}$ . The maximum contour value shown is  $3 \times 10^{-5} \text{nAm}^{-2}$ . (f) Field-aligned currents calculated using the enhanced electron density. The plot has been expanded so that only the central section is visible, as indicated by the dashed box in panels (e) and (f). Line formats have the same meaning as panel (e), however contours are now spaced at intervals of  $0.1 \text{nAm}^{-2}$ . The maximum contour value shown is  $0.3 \text{nAm}^{-2}$ .

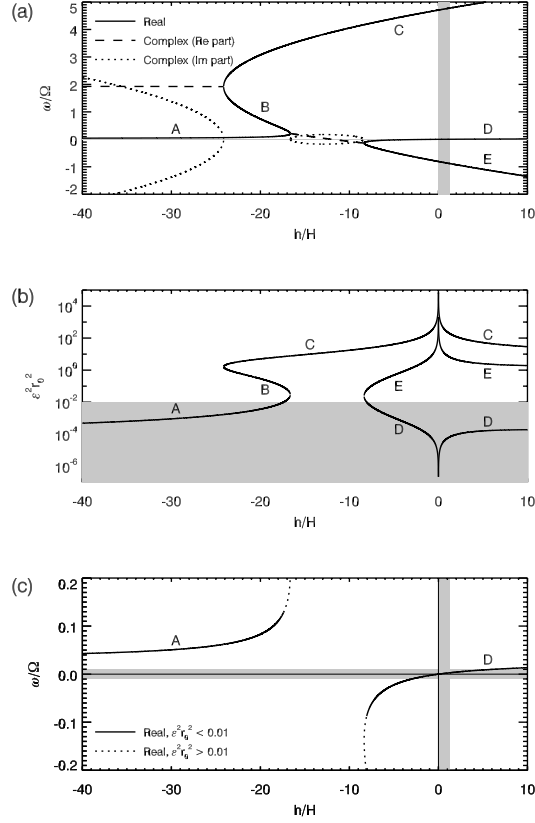


Figure 5: (a) Values of angular speed  $\omega$  as a fraction of the deep planetary angular velocity  $\Omega$  for solutions with a range of values of  $h$ . Solid lines show real solutions. Dashed and dotted lines shows complex solutions, with the real parts plotted as a dashed line and the conjugate imaginary parts of the two solutions as dotted lines. (b) Calculated values of  $\epsilon^2 r_0^2$  for the real solutions shown in panel (a). The shaded region shows values below 0.01. (c) Expanded version of panel (a) with only real solutions shown. Solid lines indicate solutions for which  $\epsilon^2 r_0^2 < 0.01$ .

389 We are wish to find steady state solutions, and so we are interested in  
390 frequencies that are real – so that they do not exponentially grow or decay  
391 – with a very small positive value of  $\omega$ . There are two regions on the graph  
392 where these conditions appear to be fulfilled – region A and the part of region  
393 D for  $h > 0$ . It is worth noting that the choice of  $h$ , rather than  $1/h$  as the  
394 abscissa is arbitrary, and so these two branches of the graph are effectively  
395 part of the same group of wave modes, and are connected at  $h = \infty$ . It is  
396 further worth noting that this branch of wave modes arises from the final term  
397 in Eq. 26, which in turn arises from the variation in latitude of the Coriolis  
398 parameter: these are therefore Rossby waves as generally understood.

399 As already discussed above, these wave solutions are only valid if  $\epsilon^2 r^2 \ll$   
400 1. Figure 5b shows this quantity calculated at  $r_0$ , for real solutions only.  
401 The region shaded in grey shows when it falls below 0.01. In this region the  
402 approximation that neglects terms involving  $\epsilon^2 r^2$  is certainly valid. It is clear  
403 that it is valid for regions A and D. Fig. 5c shows an expanded version of  
404 Fig. 5a, showing real solutions only, to more clearly show the low frequency  
405 wave modes that interest us. The solid lines show wave modes for which  
406  $\epsilon^2 r_0^2 < 0.01$ . Again, this clearly demonstrates that our approximation is valid  
407 for the low frequency sections of regions A and D. These slowly propagating  
408 modes are therefore our candidates for explaining the 10.7-hour periodicities.

#### 409 3.4. Vertical structure

410 We now investigate the vertical structure function  $F(z)$ . Taking the equa-  
411 tion derived in the Appendix (Eqn. A.20), and setting the external heating  
412 parameter  $q$  to zero, as required for free oscillations,  $F$  is described by:

$$F'' + a^2 F = 0 \tag{27}$$

413 where  $a$  is given by:

$$a^2 = \frac{\kappa}{Hh} - \frac{1}{4H^2} \quad (28)$$

414 We find that  $a$  is real if  $0 < h < h_{lim}$ , where  $h_{lim} = 4\kappa H$ , and in these circum-  
415 stances the solutions of Eqn. 27 are vertically propagating waves. Otherwise,  
416  $a = i\alpha$  is imaginary. In this case they are evanescent waves in the vertical  
417 direction and the energy is trapped. Fig. 6 shows the calculated values of  $a$   
418 and  $\alpha$  showing, by the dashed line, the narrow range of  $h$  for which waves  
419 propagate. The vertical shaded region in Fig. 5a shows the same range of  
420  $h$  for which vertical propagation is possible. Although this shows a very  
421 narrow range of possible solutions in which energy can propagate vertically,  
422 these also correspond to small values of  $\omega$  with the value at  $h_{lim}$  given by  
423  $\omega_{lim} \simeq 0.00308\Omega$ . The possible values of  $\omega$  that propagate vertically are  
424 therefore all less than  $\sim 0.308\%$  of the planetary rotation velocity. These are  
425 therefore very good candidates for explaining the 10.7-hour periodicities.

### 426 3.5. Vertical propagation

427 As already discussed, a wave in the stratosphere can only propagate into  
428 the shear layer in the lower thermosphere if it experiences a change in phase  
429 velocity that exactly cancels the westwards background flow. This is a form  
430 of a Doppler shift. Consider a wave propagating upwards from the deep  
431 atmosphere, with some initial angular speed  $\omega^*$ . If the wave is to propagate  
432 vertically, then we must have  $\omega^* \leq \omega_{lim}$ . As it rises through the atmosphere,  
433 its total angular speed in the corotating planetary frame must remain equal  
434 to  $\omega^*$ . If we represent the westwards angular speed of the gas in each layer  
435 as  $\omega_{shear}$ , then the angular speed of the perturbation relative to the gas in

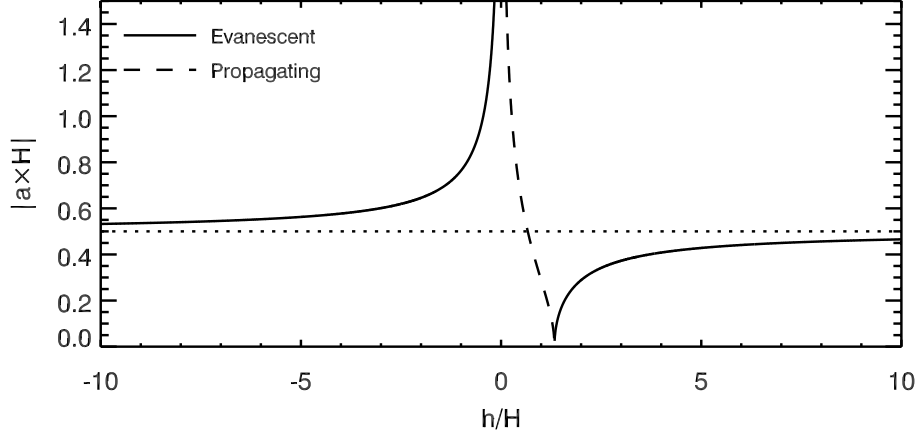


Figure 6: Calculated magnitudes of the vertical wavenumber  $a$  for Rossby wave solutions. The dashed line shows the region where  $a$  is real. The solid lines show regions where  $a = i\alpha$  is imaginary.

436 each layer must be equal to

$$\omega = \omega^* - \omega_{shear} \quad (29)$$

437 so that its westward angular speed relative to the local gas decreases as it  
 438 rises. The wave modes in the higher layers thus correspond to smaller values  
 439 of  $h$ , which also correspond to larger values of  $a$ , as illustrated in Fig. 6.  
 440 As discussed by Lindzen (1967), this means that the vertical phase velocity  
 441  $\omega/a$  tends to zero. It can therefore never reach the layer where  $\omega$  equals  
 442 zero, which is referred to as a ‘critical layer’. It must either be absorbed  
 443 or reflected at this altitude. Working out what happens in this situation  
 444 is difficult, because as  $a$  grows the wavelength decreases, and therefore the  
 445 vertical gradients of  $u$ ,  $v$  and  $\delta p$  also increase. The values of  $\delta\rho$  and  $w$   
 446 directly depend on the vertical gradient of  $\delta p$ ; this means that the values of

447  $\delta\rho$  and  $w$  tend towards infinity as we approach the critical layer, and thus  
448 the linearisation of the equations breaks down.

449 Critical layers have been well studied in the context of horizontally prop-  
450 agating Rossby waves in the Earth’s atmosphere. For example, Killworth  
451 and McIntyre (1985) describe a model in which, after a sufficiently long pe-  
452 riod of time, critical layers reflect horizontally propagating Rossby waves. A  
453 more recent study (Potter et al., 2013) also studied horizontally propagating  
454 Rossby waves and found partial reflection at critical layers. The question of  
455 what occurs when a Rossby wave impinges vertically on a critical layer has  
456 been much less well studied.

457 However, a well-studied example of a situation in which waves vertically  
458 impinge upon a critical layer is the case of the quasi-biennial oscillation in  
459 the Earth’s equatorial stratosphere (Baldwin et al., 2001). In this case, waves  
460 tend to be absorbed, modifying the existing jet by transfer of momentum.  
461 However, this is a very different situation to the one studied here, in particular  
462 involving small-scale waves rather than planetary-scale waves. It does not  
463 seem reasonable to infer by analogy that the waves represented by our model  
464 are absorbed.

465 We will therefore investigate two situations: one in which the Rossby  
466 waves are completely absorbed by the critical layer and another in which  
467 complete reflection occurs.

468 To calculate the altitude of the critical layer we ideally require a model of  
469 the shear in Saturn’s lower thermosphere and upper stratosphere. Unfortu-  
470 nately, while the existence of flow shear seems inevitable, the degree of shear  
471 in this region is unconstrained by direct observations and there are many un-

472 certainties in calculating it theoretically. Smith (2014) estimated the *relative*  
473 shear below 1000km using a simple viscous transfer model. However, the  
474 absolute neutral velocity at 1000km is very uncertain, and thus the absolute  
475 shear is difficult to estimate. Furthermore, advective processes may also be  
476 important in these regions, rendering the viscous calculation an overestimate  
477 of the shear (Smith and Aylward, 2008).

478 We therefore show in Fig. 7a a highly simplified and somewhat arbitrary  
479 illustrative model of a possible flow shear, represented by a constant flow  
480 below 600km altitude and a constant vertical shear above this altitude. The  
481 vertical dotted line labelled *A* shows an angular speed of  $\omega^* = 0.0025\Omega$ . This  
482 is smaller than  $\omega_{lim}$  and so a wave with this angular speed can propagate  
483 vertically in the deep atmosphere. At an altitude of about 700km,  $\omega_{shear} = \omega^*$   
484 and thus the wave cannot propagate beyond this altitude. The curve labelled  
485 *A* in Fig. 7b illustrates this further by showing the values of *a* and  $\alpha$  implied  
486 at each altitude by the value of  $\omega$ . The dashed line below 725km indicates  
487 that the wave can propagate vertically in this region. At 700km  $a \rightarrow \infty$ , and  
488 so this is a critical layer. Although evanescent solutions are possible above  
489 700km, the critical layer is assumed to absorb or reflect incoming waves and  
490 so no wave is set up in this region. It should be emphasised that the decision  
491 to begin the shear at 600km is entirely arbitrary – the actual critical layer  
492 may lie higher in the atmosphere, such that Rossby waves can penetrate high  
493 enough to interact with the ionosphere and generate currents.

494 In this situation, we thus have a region in which Rossby waves can freely  
495 propagate, but this region extends continuously into the deep atmosphere.  
496 Therefore any locally generated Rossby waves – possibly due to asymmetries

497 in the auroral forcing, which penetrates as deep as 700km – could propagate  
498 away into the deep atmosphere, carrying away energy. A more promising  
499 situation would be a wave source deep in the atmosphere, perhaps a persis-  
500 tent tropospheric asymmetry such as the Great White Spot (Fischer et al.,  
501 2014), which might drive Rossby waves that could propagate upwards into  
502 the stratosphere. This is the ‘open wave cavity’ model sketched in Fig. 2.

503 An alternative possibility is illustrated by the angular speeds labelled  $B$   
504 and  $C$ . These both involve  $\omega^* > \omega_{lim}$ , and so they cannot propagate in the  
505 deep atmosphere, but only above a certain altitude in the shear layer, at  
506 which point  $\omega$  falls below  $\omega_{lim}$ . At a higher altitude still, they can no longer  
507 propagate as  $\omega$  falls to zero, and there is a critical layer. The dashed lines in  
508 Fig. 7b show the altitudes where propagation is possible.

509 These situations are intriguing, because there appears to be a closed  
510 wave cavity or waveguide at high altitudes within which propagation is pos-  
511 sible. This is sketched in Fig. 8. This implies that Rossby waves could  
512 become trapped in the upper stratosphere, with the energy unable to radiate  
513 away into the deep atmosphere. Having set up an oscillation in this cavity,  
514 we would then simply need to occasionally force the upper stratosphere to  
515 counter the gradual dissipation of the trapped waves.

516 This ‘closed wave cavity’ model depends on the assumption that the crit-  
517 ical layer reflects waves. If it is a perfect reflector then a standing wave  
518 may be set up. If it is a perfect absorber then the wave would presumably  
519 be damped very rapidly. The former possibility is the most intriguing, be-  
520 cause the concept of a ‘resonant cavity’ is very attractive in explaining the  
521 uniqueness and persistence of the 10.7-hour signals.

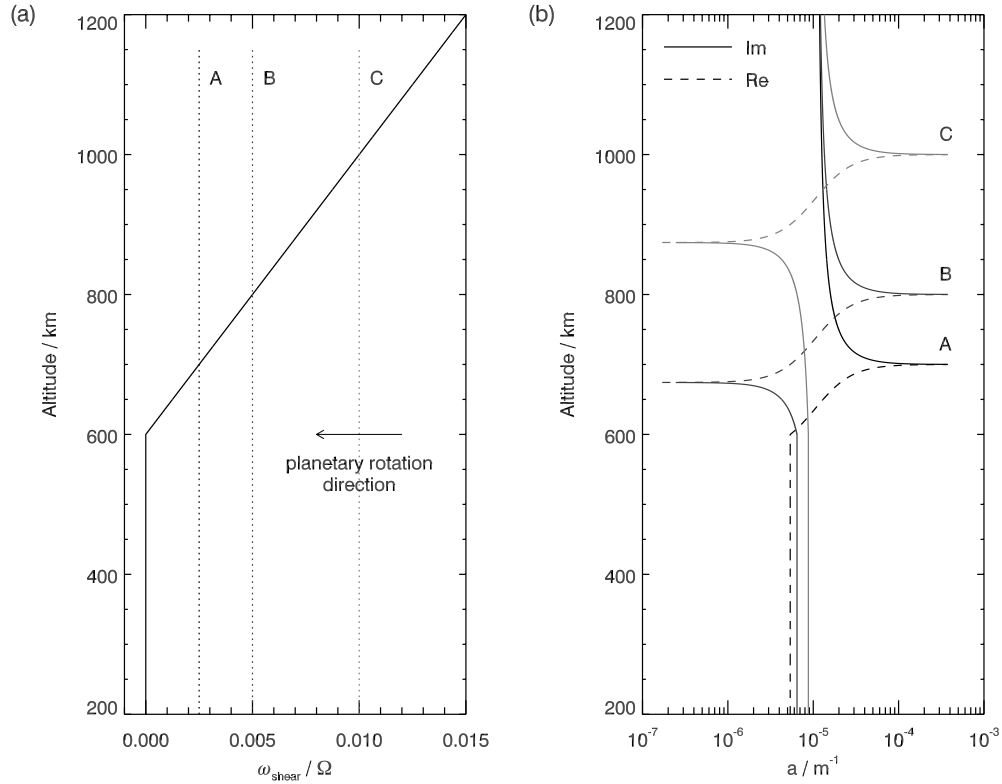


Figure 7: Shear model of the upper stratosphere and lower thermosphere. (a) The solid line shows our illustrative shear model. The vertical dashed lines labelled A, B and C show three possible angular speeds for waves propagating against this background. To emphasise that the angular speeds shown represent subcorotation of the atmosphere (i.e. westwards flow), the arrow indicates the planetary rotation direction. (b) Vertical wavenumbers implied by the exponential shear model and the angular speeds plotted in panel (a). The solid lines show regions where the vertical wavenumber is imaginary and no propagation is possible. The dashed lines show regions where the vertical wavenumber is real and waves can propagate vertically.

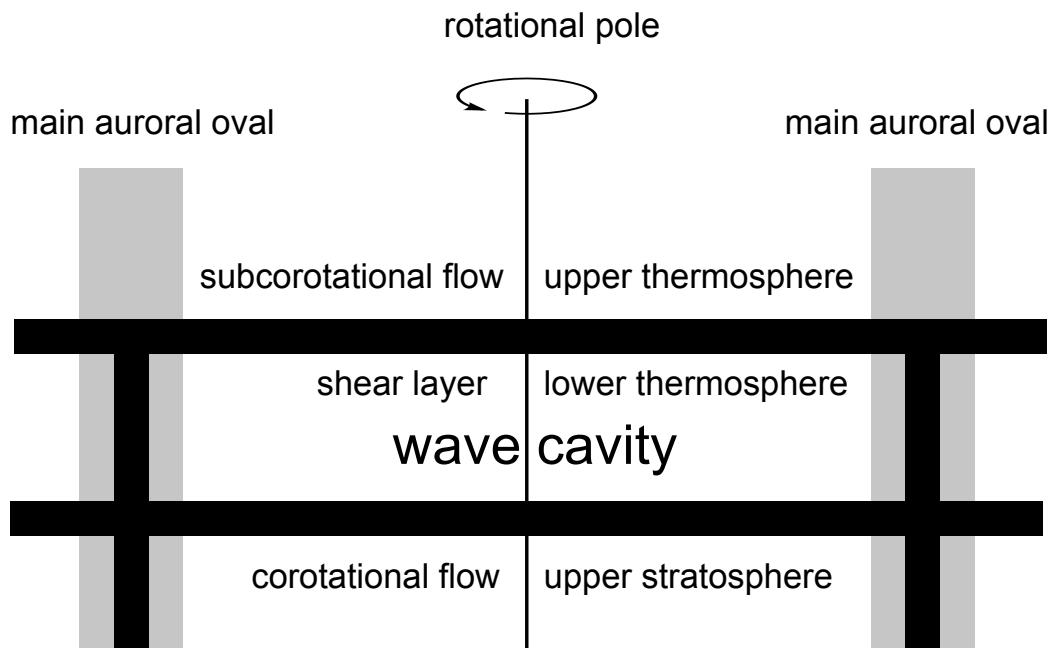


Figure 8: Sketch of alternative 'wave cavity' model, similar to Fig. 2. The wave cavity now lies between the two horizontal black bars. Rossby waves are trapped in the shear layer itself, and are unable to propagate to lower or higher altitudes.

## 522 4. Solutions

523 We now consider solutions for  $F(z)$  for open and closed wave cavity mod-  
524 els.

### 525 4.1. Open wave cavity

526 In this case we adopt one of two scenarios: either the Rossby waves  
527 originate deeper in the atmosphere and propagate upwards into the region of  
528 interest, or they are generated locally and propagate downwards into the deep  
529 atmosphere. We assume that upwards propagating waves will be absorbed  
530 by the critical layer, and so we do not have to worry about interference  
531 between waves moving in opposite directions. On this basis, since the vertical  
532 wavenumber  $a$  is real, we can represent the vertical structure simply as

$$F(z) = e^{iaz} \quad (30)$$

533 so that positive  $a$  corresponds to downwards phase propagation.

534 Inserting this into the expressions for  $u$  and  $v$  and recalculating the pre-  
535 dicted field-aligned currents, we find that we need  $v_0 \simeq 150\text{ms}^{-1}$  to generate  
536 integrated currents of  $\sim 1\text{MA}$ , as required to explain the observations. This  
537 implies peak wind speeds at  $z = 900\text{km}$  of about  $70\text{ms}^{-1}$  and a peak frac-  
538 tional pressure perturbation at  $z = 900\text{km}$  of only 0.035.

#### 539 4.1.1. Energy

540 To assess whether these values are energetically plausible, we need to  
541 estimate the vertical energy flux associated with the wave. This is achieved  
542 for atmospheric waves by calculating the product  $w\delta p$  (e.g. Mak, 2011) and

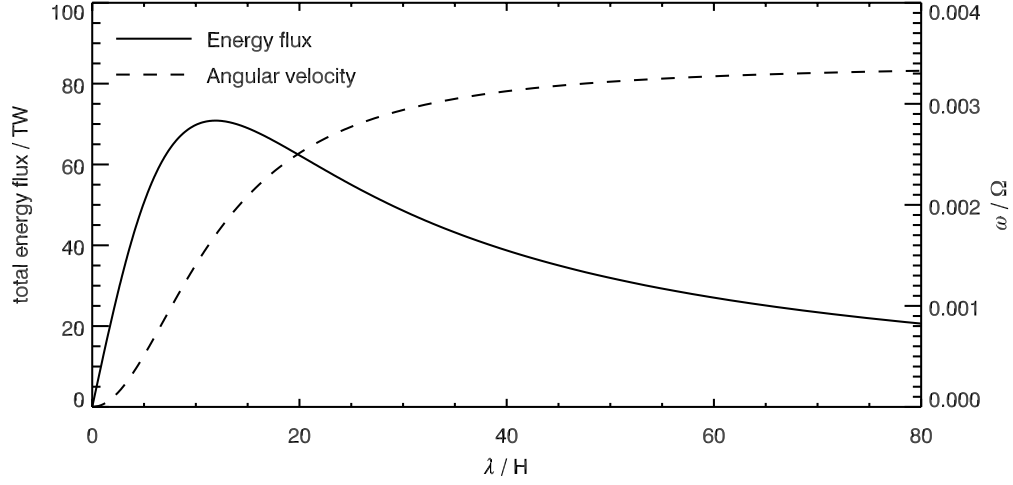


Figure 9: Dependence of total vertical energy flux on vertical wavelength. The dashed line shows the value of  $\omega$  corresponding to each wavelength.

543 averaging it over a full cycle. This yields the following expression:

$$E = \overline{w\delta p} = \frac{p_{00}\omega H^2 a}{2\kappa} \left( \frac{v_0}{v_{00}} \right)^2 K_k^2(mr, \omega) \quad (31)$$

544 This energy flux depends strongly on both  $\omega$  and  $a$ , which in turn both  
 545 depend on the equivalent depth  $h$ . Integrating over the whole of the polar  
 546 region (from the pole to  $r = 3.1 \times 10^7$ m) allows us to calculate the total  
 547 integrated flux. In Fig. 9 we show its dependence on the vertical wavelength  
 548  $\lambda = 2\pi/a$ . This shows a very large integrated energy flux of  $\sim 70$ TW for a  
 549 vertical wavelength of  $\sim 10$  scale heights. However, for shorter wavelength  
 550 disturbances a much smaller energy flux may be required. For example for  
 551 a vertical wavelength of  $H$  the energy flux is  $\sim 12$ TW and for a vertical  
 552 wavelength of  $0.1H$  it is  $\sim 1.2$ TW.

553 For the case in which the waves are generated locally and then propagate

554 downwards, we can compare these calculated powers to the energy available  
555 from particle precipitation which is a plausible energy source for generating  
556 the waves in the upper atmosphere. We can estimate this by calculating the  
557 total incident energy due to particle precipitation in the main oval. The total  
558 area of particle precipitation is an annulus of width  $\sim 1000\text{km}$  and circum-  
559 ference  $\sim 100,000\text{km}$ , yielding a surface area of  $\sim 1 \times 10^{14}\text{m}^2$ . Taken together  
560 with a precipitating energy flux of  $0.2\text{mWm}^{-2}$  in the form of  $10\text{keV}$  electrons,  
561 peaking at  $\sim 800\text{km}$  and so delivering most of that energy to our region of  
562 interest (Galand et al., 2011), this implies a total energy flux of  $\sim 0.02\text{TW}$ .  
563 The energy flux is probably even higher than this, perhaps peaking closer to  
564  $5\text{mWm}^{-2}$  (Cowley et al., 2008). This implies that  $\sim 25$  times more energy  
565 may be available, i.e. a total energy of flux of  $\sim 0.5\text{TW}$ .

566 Thus the total energy available from particle precipitation is much smaller  
567 than the maximum possible energy flux. This restricts locally generated wave  
568 modes except those with very short vertical wavelengths. However, it places  
569 no restriction on waves generated deeper in the atmosphere propagating up-  
570 wards into the upper stratosphere/lower thermosphere, for which the energy  
571 source is unknown.

#### 572 *4.1.2. Consistency with assumptions*

573 We can use these solutions to assess consistency with our main simplifying  
574 assumptions.

575 First, our assumption of hydrostatic equilibrium is related to the vertical  
576 motion associated with the waves. If the vertical amplitude of the waves  
577 is comparable to the scale height of the atmosphere then it seems unrea-  
578 sonable to treat the waves as a perturbation to a hydrostatic equilibrium

579 state. The vertical amplitude is given approximately by  $w_0/\omega$ , which, using  
 580  $v_0 = 150\text{ms}^{-1}$  and  $v_{00} = 230\text{ms}^{-1}$  yields a value of  $\sim 2H$ . This means that  
 581 oscillations of the required amplitude are probably not sufficiently small for  
 582 hydrostatic equilibrium to hold.

583 Second, we assumed that the perturbations were small enough to allow  
 584 linearisation of the equations. In practice, this amounts to neglecting advec-  
 585 tion of the perturbed quantities by the wind perturbations themselves. This  
 586 is reasonable if the time for the perturbed wind to cross the polar cap is much  
 587 smaller than the time period of the wave. This amounts to the condition:

$$v \ll \omega r_0 \simeq 7\text{ms}^{-1} \quad (32)$$

588 where we have used  $\omega = 0.003\Omega_0$ . The wind speeds predicted with  $v_0 =$   
 589  $150\text{ms}^{-1}$  are considerably greater than this, indicating that linearisation is  
 590 also not a valid assumption.

591 While neither of these assumptions are strictly valid for the conditions  
 592 required to produce  $\sim 1\text{MA}$  currents, this of course does not rule out the  
 593 possibility that similar non-hydrostatic and non-linear structures may be  
 594 present. However, it does mean that our results must be treated with greater  
 595 caution.

#### 596 *4.2. Closed wave cavity*

597 The alternative concept of a closed wave cavity in which energy is trapped  
 598 is more attractive than the open wave cavity for two reasons:

- 599 1. If the energy is trapped then a smaller input of energy will be required  
 600 to sustain the wave.

601 2. The existence of resonant states in the closed cavity is an attractive  
 602 explanation of the uniqueness and persistence of the  $\sim 10.7$  hour signal.

603 A full analysis is beyond the scope of this paper because it would require  
 604 a self-consistent treatment of the shear itself. In lieu of such an analysis, we  
 605 will present an illustrative calculation, employing the following assumptions:

- 606 1. We assume that the critical layer acts as a rigid reflecting ‘lid’ at which  
 607 the values of  $u$ ,  $v$  and  $\delta p$  drop to zero. This means that  $w$  and  $\delta\rho$  will  
 608 not necessarily be zero at this altitude.
- 609 2. We use a simplified three layer model of the flow shear. The lowest  
 610 layer, representing the deep atmosphere, is in perfect corotation. The  
 611 second layer, representing the lower regions of the shear layer, has a  
 612 subcorotation velocity of  $\omega_{sh}$  and a width of  $\Delta$ . The upper layer, above  
 613 the critical layer at  $z = z_c$ , has a subcorotation velocity which is con-  
 614 siderably greater than  $\omega_{sh}$ , and is effectively inaccessible to the waves.
- 615 3. At the discontinuity between the lower and middle layers, we assume  
 616 continuity of  $F$  and  $F'$ . These conditions guarantee continuity of  $u$  and  
 617  $v$  and their vertical derivatives. It is impossible to guarantee continuity  
 618 of  $\delta p$ ,  $\delta\rho$  and  $w$  because these variables depend on  $K_k$ , which is a  
 619 function of  $\omega$ , which by necessity varies between the layers.

620 On the basis of these assumptions, a standing wave develops in the middle  
 621 layer, and we find the following solution:

$$F(z) = \begin{cases} 0, & \text{if } z \geq z_c. \\ \sin a(z_c - z), & \text{if } z_c - \Delta \leq z \leq z_c. \\ \sin(a\Delta)e^{-\alpha(z_c - \Delta)}e^{\alpha z}, & \text{if } z \leq z_c - \Delta. \end{cases} \quad (33)$$

622 with the following condition:

$$\tan(a\Delta) = -\frac{a}{\alpha} \quad (34)$$

623 where  $a$  is the wavenumber in the middle layer and  $i\alpha$  is the wavenumber in  
624 the lower layer. The value of  $\Delta$  is fixed by the three layer shear model. To  
625 find a solution, we must adjust  $\omega^*$  (the angular speed of the wave relative  
626 to the corotating deep atmosphere), on which  $a$  and  $\alpha$  depend, until we find  
627 a value for which the condition is satisfied. This implies that only specific  
628 wave modes are allowed.

629 We now investigate a concrete example of this three-layer model. We use  
630  $\Delta = 200\text{km}$  and  $z_c = 900\text{km}$ . We then take  $\omega_{sh} = 0.0030\Omega$  within the middle  
631 layer. The angular speed of the shear in the upper layer is unimportant,  
632 provided it is large enough to inhibit wave propagation; for the purposes of  
633 illustration we take it to be  $0.012\Omega$ .

634 In this case there are three possible solutions, corresponding to total  
635 angular speeds relative to corotation ( $\omega^*$ ) of 0.46%, 0.35% and 0.32% of  $\Omega_S$   
636 and relative angular speeds within the shear layer ( $\omega$ ) of 0.16%, 0.049% and  
637 0.021%. These solutions are shown by the vertical solid, dashed and dot-dash  
638 lines in Fig. 10a. We have deliberately chosen a value of  $\omega_{sh}$  that gives exactly  
639 three solutions. The number of solutions increases as  $\omega_{sh}$  approaches  $\omega_{lim}$ ;  
640 for values of  $\omega_{sh} > \omega_{lim}$  there are an infinite number of possible solutions,  
641 most of which are very short-wavelength.

642 The profiles of  $F(z)$  for the three solutions are shown in Fig. 10b us-  
643 ing the same line formats as Fig. 10a. This shows that for solutions with  
644 a smaller total angular speed, the vertical wavelength in the shear layer de-  
645 creases, while the exponential scale length below the shear layer increases,

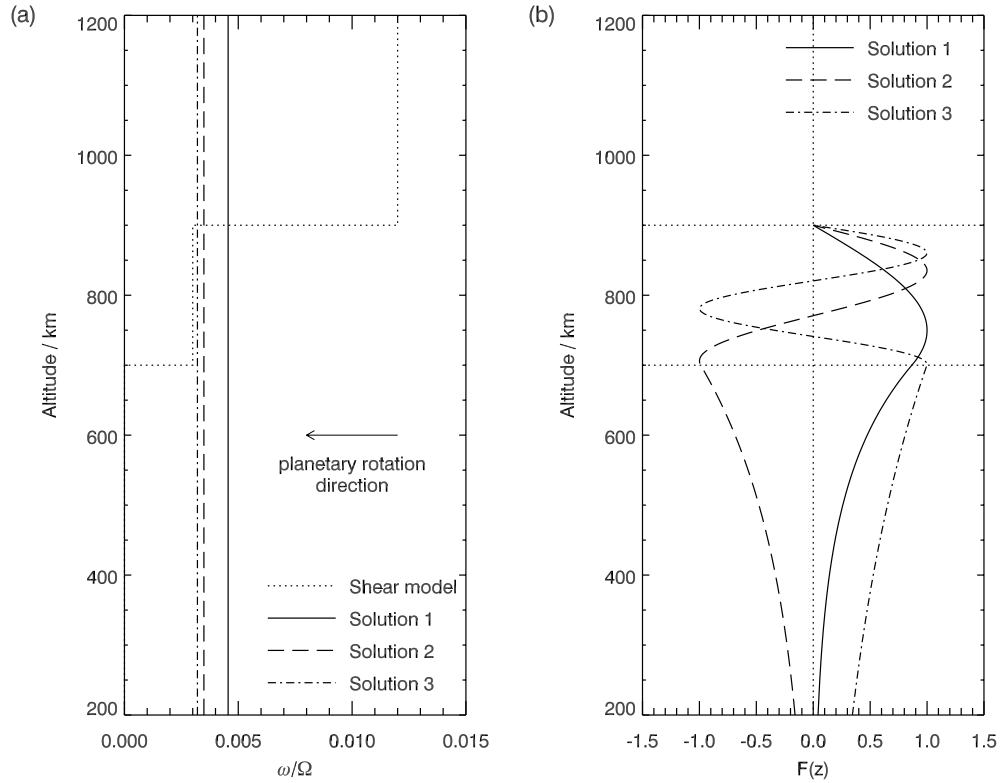


Figure 10: Solutions for the three layer model. Panel (a) shows the three layer shear model as a dotted line. The vertical solid, dashed and dot-dash lines show the total angular speed of the three possible wave solutions in the corotating planetary reference frame. To emphasise that the angular speeds shown represent subcorotation of the atmosphere (i.e. westwards flow), the arrow indicates the planetary rotation direction. Panel (b) shows the calculated values of  $F$  for these three models, using the same line formats.

646 such that Solution 1 has a broad peak in the shear layer whose amplitude  
647 drops relatively rapidly to very small values at 200km, whereas Solution 3  
648 has three much narrower peaks in the shear layer and a much more gradual  
649 drop in amplitude below the shear layer, which falls to only about one half  
650 of its peak value at 200km.

651 The discrete number of wave modes produced by this analysis provides  
652 a potentially elegant mechanism for selecting specific frequencies, explaining  
653 the uniqueness of the 10.7-hour structure. However, it is clear that further  
654 work is required to demonstrate that such wave modes can exist in real  
655 sheared flows.

## 656 5. Conclusions

657 We have applied the theory of Haurwitz (1975) to find planetary wave  
658 solutions for the polar upper atmosphere of Saturn. Some of the solutions  
659 have the properties necessary to explain the 10.7-hour periodicities:

- 660 • There exist solutions for slowly westwards-propagating Rossby waves  
661 whose total angular velocity is slightly below that of the deep atmo-  
662 sphere.
- 663 • A broad spectrum of waves with different angular velocities are possible,  
664 thus permitting the total angular velocity to vary on a timescale of  
665 months if the background conditions change.
- 666 • The flow pattern associated with the wave is of exactly the form pro-  
667 posed to explain the periodicities, and so the field-aligned currents  
668 generated by the wave are also of the correct form.

669 The existence of a spectrum of wave modes has directed us to propose  
670 mechanisms for restricting the possible wave modes or allowing one mode to  
671 become dominant, all of which require further investigation:

- 672 • The shear layer in the lower thermosphere is proposed to act either as a  
673 ‘lid’ to inhibit propagation of waves to higher altitudes, or as a ‘cavity’  
674 that traps waves in a restricted altitude range.
- 675 • The enhanced ion drag at the latitude of the main auroral oval is pro-  
676 posed to inhibit zonal winds, prejudicing the growth of wave modes  
677 with a nodal line in the zonal winds at this latitude.

678 The principal limitations of our model are as follows:

- 679 • Wind speeds of  $\sim 70\text{ms}^{-1}$  are required to generate currents of the order  
680 of 1MA, as required to explain the magnetospheric observations, but  
681 speeds of this magnitude violate the underlying assumptions of the  
682 model (hydrostatic equilibrium and linearisation).
- 683 • We do not have a good model of the neutral wind shear, and so cannot  
684 accurately estimate the altitude to which Rossby waves can propagate.
- 685 • We do not have a good understanding of the behaviour of Rossby waves  
686 impinging vertically on a critical layer, and thus do not know if they  
687 are absorbed, reflected. or partially reflected.

688 Other questions which remain to be answered include:

- 689 • Do the details of the field-aligned currents driven by the wave structure  
690 match the magnetospheric observations?

- 691 • To what extent do seasonal variations in the background conditions,  
692 for example temperature, affect the predicted values of  $\omega$ , and do these  
693 variations explain the observations?
- 694 • What are the effects of the various damping processes on the wave  
695 structure?
- 696 • Is it possible for perturbations to the main auroral oval, driven by the  
697 wave structure, to feed back and provide energy to maintain the wave  
698 structure?

## 699 **Acknowledgements**

700 LCR was supported by STFCs UCL Astrophysics Consolidated grant  
701 ST/J001511/1.

## 702 **Appendix A.**

703 The following derivation closely follows that of Haurwitz (1975).

704 To begin the process of solving Eqns. 6-10 we make the following standard  
705 substitutions which greatly simplify the manipulations that follow:

$$u' = \rho_0^{1/2} u \tag{A.1}$$

$$v' = \rho_0^{1/2} v \tag{A.2}$$

$$w' = \rho_0^{1/2} w \tag{A.3}$$

$$\delta p' = \rho_0^{-1/2} \delta p \tag{A.4}$$

$$\delta \rho' = \rho_0^{-1/2} \delta \rho \tag{A.5}$$

706 Substituting all of the above into Eqns. 6-10 yields the following:

$$i\omega u' - fv' = -\frac{ik}{r}\delta p' \quad (\text{A.6})$$

707

$$i\omega v' + fu' = \frac{\partial \delta p'}{\partial r} \quad (\text{A.7})$$

708

$$\frac{\partial \delta p'}{\partial z} - \frac{1}{2H}\delta p' = -g\delta \rho' \quad (\text{A.8})$$

709

$$i\omega \delta \rho' - \frac{1}{2H}w' + \frac{ik}{r}u' - \frac{1}{r}\frac{\partial v'r}{\partial r} + \frac{\partial w'}{\partial z} = 0 \quad (\text{A.9})$$

710

$$i\omega \delta p' = i\omega \gamma g H \delta \rho' - g(\gamma - 1)w' + (\gamma - 1)q\rho_0^{1/2} \quad (\text{A.10})$$

711 We can combine the equations to above to eliminate  $w'$ ,  $\delta \rho'$  and  $u'$ , yielding

712 two equations involving  $v'$ ,  $\delta p'$  and the forcing function  $q$  alone:

$$v'(f^2 - \omega^2) = \frac{ikf}{r}\delta p' + i\omega \frac{\partial \delta p'}{\partial r} \quad (\text{A.11})$$

$$\begin{aligned} \frac{\omega^2 H}{\kappa} \left[ \frac{\partial^2}{\partial z^2} + \left( -\frac{1}{4H^2} + \frac{k^2 \kappa g}{Hr^2 \omega^2} \right) \right] \delta p' + \\ i\omega \left[ \frac{\partial}{\partial z} - \frac{1}{2H} \right] (\rho_0^{1/2} q) - i\omega g \left( \frac{1}{r} \frac{\partial v'r}{\partial r} - \frac{fk}{r\omega} v' \right) = 0 \end{aligned} \quad (\text{A.12})$$

713

Here  $\kappa = (\gamma - 1)/\gamma$ . We then separate variables, defining:

$$u' = F(z)U(r) \quad (\text{A.13})$$

$$v' = F(z)\frac{V(r)}{r} \quad (\text{A.14})$$

$$\delta p' = F(z)P(r) \quad (\text{A.15})$$

$$q = iQ(z)P(r) \quad (\text{A.16})$$

714 where it is clear that we have assumed that  $u'$ ,  $v'$  and  $\delta p'$  have the same  
715  $z$ -dependence.

716 Substituting Eqns. A.13 into Eqn. A.11 we obtain:

$$V(f^2 - \omega^2) = ikfP + i\omega rP' \quad (\text{A.17})$$

717 and further substituting Eqns. A.13 into Eqn. A.12 we obtain two equations  
718 by defining a separation constant  $h$ :

$$-\frac{1}{r} \frac{V'}{P} + \frac{fk}{\omega r^2} \frac{V}{P} - \frac{ik^2}{\omega r^2} = -\frac{i\omega}{gh} \quad (\text{A.18})$$

719

$$\frac{i\omega H}{g\kappa} \left[ \frac{F''}{F} - \frac{1}{4H^2} \right] - \frac{i}{gF} \left[ \frac{\partial}{\partial z} - \frac{1}{2H} \right] Q\rho_0^{1/2} = -\frac{i\omega}{gh} \quad (\text{A.19})$$

720 In these equations a prime on  $F$  indicates differentiation with respect to  $z$   
721 and primes on  $V$  and  $P$  imply differentiation with respect to  $r$ .

722 Equation A.19 can be rearranged to yield the following second order equa-  
723 tion for  $F$ :

$$F'' + \left[ \frac{\kappa}{Hh} - \frac{1}{4H^2} \right] F = \frac{\kappa}{\omega H} \left[ \frac{\partial}{\partial z} - \frac{1}{2H} \right] Q\rho_0^{1/2} \quad (\text{A.20})$$

724 Setting  $Q = 0$  in this expression gives Equation 27, appropriate for free  
725 oscillations, discussion of which is continued in Section 3.4.

Combining Equations A.17 and A.18 to eliminate  $P$  yields a second order differential equation for  $V$ :

$$V'' + \frac{1}{r} \frac{1 + \epsilon^2 r^2}{1 - \epsilon^2 r^2} V' + \left[ -\frac{k}{\omega r} \frac{\partial f}{\partial r} - \frac{(f^2 - \omega^2)}{gh} - \frac{2f\omega}{ghk(1 - \epsilon^2 r^2)} - \frac{k^2}{r^2} \right] V = 0 \quad (\text{A.21})$$

726 use of Equation A.7 and A.18 yields equations for  $U$  and  $P$  in terms of  $V$ :

$$(1 - \epsilon^2 r^2)U = \epsilon^2 r^2 \frac{ifV}{\omega r} - \frac{iV'}{k} \quad (\text{A.22})$$

727

$$(1 - \epsilon^2 r^2)P = -\frac{ifV}{k} + \frac{i\omega r V'}{k^2} \quad (\text{A.23})$$

728 where

$$\epsilon^2 = \frac{\omega^2}{ghk^2} \quad (\text{A.24})$$

729 These equations are too complex to permit simple analytic solutions. We  
 730 now make two approximations that simplify matters considerably. Firstly,  
 731 we restrict ourselves to circumstances in which  $\epsilon^2 r^2 \ll 1$ , so that we can  
 732 neglect terms involving this factor. We will only consider solutions that  
 733 satisfy this condition; this is demonstrated in the main text.

734 Secondly, we consider the terms involving the Coriolis parameter  $f$ , given  
 735 by Eqn. 5. Across the range of latitudes in which we are interested, there is  
 736 little variation in this parameter. It is thus reasonable to insert a constant  
 737 value  $f_0$  to reduce the complexity of our expressions. We choose the value at  
 738 the latitude of the main auroral oval,  $r_0$ :

$$f_0 = 2\Omega \left( 1 - \frac{r_0^2}{2R_c^2} \right) \quad (\text{A.25})$$

739 However, there is one term in Eqn A.21 that explicitly depends on the radial  
 740 derivative of  $f$ . The radial derivative is approximately:

$$\frac{\partial f}{\partial r} \simeq -\frac{2\Omega r}{R_c^2} \quad (\text{A.26})$$

741 and we insert this expression into Eqn. A.21.

742 Making these approximations, the horizontal structure equations reduce  
 743 to:

$$V'' + \frac{1}{r}V' + \left[ m^2 - \frac{k^2}{r^2} \right] V = 0 \quad (\text{A.27})$$

744

$$U = -\frac{iV'}{k} \quad (\text{A.28})$$

745

$$P = -\frac{ifV}{k} + \frac{i\omega rV'}{k^2} \quad (\text{A.29})$$

746 where

$$m^2 = \frac{2\Omega k}{R_c^2 \omega} - \frac{(f_0^2 - \omega^2)}{gh} - \frac{2f_0\omega}{ghk} \quad (\text{A.30})$$

747 The first equation is a form of Bessel's equation, and solutions that are finite  
 748 at the pole can thus be written in terms of Bessel functions of the first kind  
 749  $J_k$ :

$$V = V_0 J_k(mr) \quad (\text{A.31})$$

$$U = -\frac{imV_0}{k} J'_k(mr) \quad (\text{A.32})$$

$$P = -\frac{if_0V_0}{k} K_k(mr, \omega) \quad (\text{A.33})$$

750 where to simplify these expressions we have defined an additional function  
 751  $K_k$ :

$$K_k(mr, \omega) = J_k(mr) - \frac{\omega mr}{f_0 k} J'_k(mr) \quad (\text{A.34})$$

752 Provided that  $\omega \ll f$  (true for all slowly propagating solutions that are  
 753 relevant here) and if  $mr$  and  $k$  are of order unity (also true for all situations  
 754 considered here), the second term in the equation for  $P$  is much smaller than  
 755 the first and thus  $K_k \simeq J_k$ .

756 Dimensional considerations prompt us to relate  $V_0$  to characteristic ve-  
757 locities  $u_0$  and  $v_0$  according to:

$$v_0 = ku_0 = \rho_{00}^{-1/2} V_0 m \quad (\text{A.35})$$

758 Combing all of these expressions to eliminate  $V$ ,  $U$  and  $P$  yields Equations 18-  
759 21, discussion of which continues in the main text.

## 760 References

761 J. D. Anderson and G. Schubert. Saturn's Gravitational Field, Internal  
762 Rotation, and Interior Structure. *Science*, 317:1384–, September 2007.  
763 doi:10.1126/science.1144835.

764 S. V. Badman, N. Achilleos, K. H. Baines, R. H. Brown, E. J. Bunce, M. K.  
765 Dougherty, H. Melin, J. D. Nichols, and T. Stallard. Location of Saturn's  
766 northern infrared aurora determined from Cassini VIMS images. *Geophys.*  
767 *Res. Lett.*, 38:L03102, February 2011. doi:10.1029/2010GL046193.

768 M. P. Baldwin, L. J. Gray, T. J. Dunkerton, K. Hamilton, P. H. Haynes, W. J.  
769 Randel, J. R. Holton, M. J. Alexander, I. Hirota, T. Horinouchi, D. B. A.  
770 Jones, J. S. Kinnersley, C. Marquardt, K. Sato, and M. Takahashi. The  
771 quasi-biennial oscillation. *Reviews of Geophysics*, 39:179–229, May 2001.  
772 doi:10.1029/1999RG000073.

773 A. F. C. Bridger and D. E. Stevens. Long Atmospheric Waves and  
774 the Polar-Plane Approximation to the Earth's Spherical Geometry.  
775 *Journal of Atmospheric Science*, 37:534–544, 1980. doi:10.1175/1520-  
776 0469(1980)037<0534:LAWATP>2.0.CO;2.

- 777 J. F. Carbary and D. G. Mitchell. Periodicities in Saturn’s magnetosphere.  
778 *Reviews of Geophysics*, 51:1–30, January 2013. doi:10.1002/rog.20006.
- 779 B. J. Conrath, P. J. Gierasch, and S. S. Leroy. Temperature and circulation  
780 in the stratosphere of the outer planets. *Icarus*, 83:255–281, February 1990.  
781 doi:10.1016/0019-1035(90)90068-K.
- 782 S. W. H. Cowley and G. Provan. Saturn’s magnetospheric planetary  
783 period oscillations, neutral atmosphere circulation, and thunderstorm  
784 activity: Implications, or otherwise, for physical links. *Journal of*  
785 *Geophysical Research (Space Physics)*, 118:7246–7261, November 2013.  
786 doi:10.1002/2013JA019200.
- 787 S. W. H. Cowley, C. S. Arridge, E. J. Bunce, J. T. Clarke, A. J. Coates, M. K.  
788 Dougherty, J.-C. Gérard, D. Grodent, J. D. Nichols, and D. L. Talboys.  
789 Auroral current systems in Saturn’s magnetosphere: comparison of theo-  
790 retical models with Cassini and HST observations. *Annales Geophysicae*,  
791 26:2613–2630, September 2008. doi:10.5194/angeo-26-2613-2008.
- 792 G. Fischer, S.-Y. Ye, J. B. Groene, A. P. Ingersoll, K. M. Sayanagi, J. D.  
793 Menietti, W. S. Kurth, and D. A. Gurnett. A possible influence of the  
794 Great White Spot on Saturn kilometric radiation periodicity. *Annales*  
795 *Geophysicae*, 32:1463–1476, December 2014. doi:10.5194/angeo-32-1463-  
796 2014.
- 797 M. Galand, L. Moore, I. Mueller-Wodarg, M. Mendillo, and S. Miller. Re-  
798 sponse of Saturn’s auroral ionosphere to electron precipitation: Elec-  
799 tron density, electron temperature, and electrical conductivity. *Journal*

- 800 *of Geophysical Research (Space Physics)*, 116:A09306, September 2011.  
801 doi:10.1029/2010JA016412.
- 802 D. A. Gurnett, J. B. Groene, A. M. Persoon, J. D. Menietti, S.-Y. Ye, W. S.  
803 Kurth, R. J. MacDowall, and A. Lecacheux. The reversal of the rotational  
804 modulation rates of the north and south components of Saturn kilometric  
805 radiation near equinox. *Geophys. Res. Lett.*, 37:L24101, December 2010.  
806 doi:10.1029/2010GL045796.
- 807 B. Haurwitz. Long circumpolar atmospheric waves. *Archiv fr Me-*  
808 *teorologie, Geophysik und Bioklimatologie, Serie A*, 24:1–18, 1975.  
809 doi:10.1007/BF02247554.
- 810 J. T. Houghton. *The physics of atmospheres*. Cambridge University Press,  
811 1986.
- 812 G. J. Hunt, S. W. H. Cowley, G. Provan, E. J. Bunce, I. I. Alexeev,  
813 E. S. Belenkaya, V. V. Kalegaev, M. K. Dougherty, and A. J. Coates.  
814 Field-aligned currents in Saturn’s southern nightside magnetosphere: Sub-  
815 corotation and planetary period oscillation components. *Journal of*  
816 *Geophysical Research (Space Physics)*, 119:9847–9899, December 2014.  
817 doi:10.1002/2014JA020506.
- 818 X. Jia and M. G. Kivelson. Driving Saturn’s magnetospheric periodici-  
819 ties from the upper atmosphere/ionosphere: Magnetotail response to dual  
820 sources. *Journal of Geophysical Research (Space Physics)*, 117:A11219,  
821 November 2012. doi:10.1029/2012JA018183.

- 822 X. Jia, M. G. Kivelson, and T. I. Gombosi. Driving Saturn's magne-  
823 topheric periodicities from the upper atmosphere/ionosphere. *Jour-*  
824 *nal of Geophysical Research (Space Physics)*, 117:A04215, April 2012.  
825 doi:10.1029/2011JA017367.
- 826 P. D. Killworth and M. E. McIntyre. Do Rossby-wave critical layers absorb,  
827 reflect or over-reflect? *Journal of Fluid Mechanics*, 161:449–492, 1985.  
828 doi:10.1017/S0022112085003019.
- 829 J. W. Leachman, R. T. Jacobsen, S. G. Penoncello, and E. W. Lemmon.  
830 Fundamental equations of state for parahydrogen, normal hydrogen, and  
831 orthohydrogen. *Journal of Physical and Chemical Reference Data*, 38(3):  
832 721–748, 2009. doi:10.1063/1.3160306.
- 833 R. D. Lindzen. Planetary Waves on Beta-Planes. *Monthly Weather Review*,  
834 95:441, 1967. doi:10.1175/1520-0493(1967)095<0441:PWOBP>2.3.CO;2.
- 835 R. S. Lindzen and S. Chapman. Atmospheric Tides. *Space Science Reviews*,  
836 10:3–188, October 1969. doi:10.1007/BF00171584.
- 837 M. Mak. *Atmospheric Dynamics*. Cambridge University Press, 2011.
- 838 J. I. Moses, B. Bézard, E. Lellouch, G. R. Gladstone, H. Feuchtgruber, and  
839 M. Allen. Photochemistry of Saturn's Atmosphere. I. Hydrocarbon Chem-  
840 istry and Comparisons with ISO Observations. *Icarus*, 143:244–298, Febru-  
841 ary 2000. doi:10.1006/icar.1999.6270.
- 842 I. C. F. Müller-Wodarg, M. Mendillo, R. V. Yelle, and A. D. Aylward. A  
843 global circulation model of Saturn's thermosphere. *Icarus*, 180:147–160,  
844 January 2006. doi:10.1016/j.icarus.2005.09.002.

- 845 J. D. Nichols, S. V. Badman, E. J. Bunce, J. T. Clarke, S. W. H. Cowley,  
846 F. J. Crary, M. K. Dougherty, J.-C. Gérard, D. Grodent, K. C. Hansen,  
847 W. S. Kurth, D. G. Mitchell, W. R. Pryor, T. S. Stallard, D. L. Talboys,  
848 and S. Wannawichian. Saturn’s equinoctial auroras. *Geophys. Res. Lett.*,  
849 36:L24102, December 2009. doi:10.1029/2009GL041491.
- 850 S. F. Potter, T. Spengler, and I. M. Held. Reflection of Barotropic Rossby  
851 Waves in Sheared Flow and Validity of the WKB Approximation. *Journal*  
852 *of Atmospheric Sciences*, 70:2170–2178, July 2013. doi:10.1175/JAS-D-12-  
853 0315.1.
- 854 P. L. Read, B. J. Conrath, L. N. Fletcher, P. J. Gierasch, A. A. Simon-Miller,  
855 and L. C. Zuchowski. Mapping potential vorticity dynamics on saturn:  
856 Zonal mean circulation from Cassini and Voyager data. *Planetary & Space*  
857 *Science*, 57:1682–1698, December 2009a. doi:10.1016/j.pss.2009.03.004.
- 858 P. L. Read, T. E. Dowling, and G. Schubert. Saturn’s rotation period from  
859 its atmospheric planetary-wave configuration. *Nature*, 460:608–610, July  
860 2009b. doi:10.1038/nature08194.
- 861 F. W. Sears and G. L. Salinger. *Thermodynamics, Kinetic Theory, and*  
862 *Statistical Thermodynamics*. Addison-Wesley, 1975.
- 863 C. G. A. Smith. Periodic modulation of gas giant magnetospheres by the  
864 neutral upper atmosphere. *Annales Geophysicae*, 24:2709–2717, October  
865 2006. doi:10.5194/angeo-24-2709-2006.
- 866 C. G. A. Smith. A Saturnian cam current system driven by asymmet-

- 867 ric thermospheric heating. *MNRAS*, 410:2315–2328, February 2011.  
868 doi:10.1111/j.1365-2966.2010.17602.x.
- 869 C. G. A. Smith. Electrodynamic coupling of Jupiter’s thermosphere and  
870 stratosphere: A new source of thermospheric heating? *Icarus*, 226:923–  
871 944, September 2013. doi:10.1016/j.icarus.2013.07.001.
- 872 C. G. A. Smith. On the nature and location of the proposed twin vortex sys-  
873 tems in Saturn’s polar upper atmosphere. *Journal of Geophysical Research*  
874 (*Space Physics*), 2014. doi:10.1002/2014JA019934.
- 875 C. G. A. Smith and N. Achilleos. Axial symmetry breaking of Saturn’s  
876 thermosphere. *MNRAS*, 422:1460–1488, May 2012. doi:10.1111/j.1365-  
877 2966.2012.20719.x.
- 878 C. G. A. Smith and A. D. Aylward. Coupled rotational dynamics of Saturn’s  
879 thermosphere and magnetosphere: a thermospheric modelling study. *An-*  
880 *nales Geophysicae*, 26:1007–1027, May 2008. doi:10.5194/angeo-26-1007-  
881 2008.
- 882 C. G. A. Smith, A. D. Aylward, S. Miller, and I. C. F. Müller-Wodarg. Polar  
883 heating in Saturn’s thermosphere. *Annales Geophysicae*, pages 2465–2477,  
884 2005. doi:10.5194/angeo-23-2465-2005.
- 885 D. J. Southwood and S. W. H. Cowley. The origin of Saturn’s mag-  
886 netic periodicities: Northern and southern current systems. *Journal*  
887 *of Geophysical Research (Space Physics)*, 119:1563–1571, March 2014.  
888 doi:10.1002/2013JA019632.

889 T. S. Stallard, S. Miller, L. M. Trafton, T. R. Geballe, and R. D. Joseph.  
890 Ion winds in Saturn's southern auroral/polar region. *Icarus*, 167:204–211,  
891 January 2004. doi:10.1016/j.icarus.2003.09.006.